5 Induced polarization and self-potential

The induced-polarization (IP) and and self-potential (SP) methods of geophysical exploration are based on measurements, normally made at the surface of the Earth, of electric potentials that are associated with subsurface charge distributions. In the IP method, the charge distributions are induced by an application of external electrical energy. In the SP method, subsurface charge distributions are maintained by persistent, natural electrochemical processes.

Consider the hypothetical situation shown in Figure 5.1 in which electrical charges are distributed unevenly within the subsurface. Charge accumulations are portrayed schematically in the figure as positive and negative "charge centers." The charges may be volumetrically distributed or they may reside on mineral surfaces and other interfaces. In either case, the regions where charge is concentrated can be viewed as the spatially extended terminals of a kind of natural battery, or geobattery. The sketch shown in the figure greatly simplifies the realistic charge distributions that occur within actual geological formations but it is instructive for the present purpose. Electrical energy supplied from an external source, or energy that naturally arises from a persistent electrochemical process, is required to maintain the "out-of-equilibrium" charge distributions shown in Figure 5.1. Without an energy input, they would rapidly neutralize in the presence of the conductive host medium, and the geobattery would soon discharge.

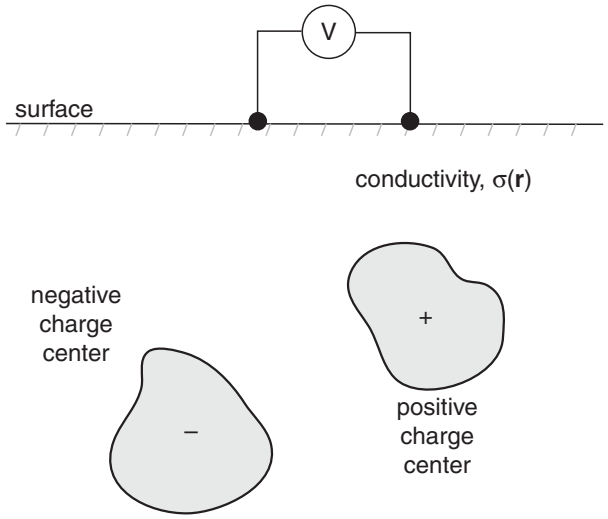

Figure 5.1 Generic subsurface charge polarization.

5.1 Induced polarization (IP): introduction

Suppose a standard resistivity experiment (see Chapter 4) is performed in which the current I is suddenly switched off at time $t = 0$. The voltage across any pair of potential electrodes normally drops instantaneously to zero. However, if the ground is *polarizable*, the voltage drops rapidly from its initial value V_0 to a non-zero value V_1 and thereafter decays slowly, often with a characteristic *stretched-exponential* shape of the form $\sim t\exp(-at^{\beta})$ with $0 < \beta < 1$, as shown in Figure 5.2. This transient behavior is known as the time-domain *IP effect*. Notice that the IP decay curve cannot be simply explained by an effective capacitance C in series with an effective resistance R in an equivalent RC circuit of the Earth. The discharge of such a capacitance after current switch off generates a transient voltage that decays purely exponentially as $\sim\exp(-t/RC)$ (Tipler, 1982), not according to a stretched exponential law.

There is not widespread agreement amongst geophysicists as to the physical explanation for the stretched-exponential shape of the transient IP decay. Significantly however, a stretched-exponential function is nothing more than a linear superposition of ordinary exponential decays. Stretched-exponential functions have been shown by many authors (e.g. Frisch and Sornette, 1997) to generally describe the macroscopic relaxation of a hierarchical or disordered system, each component of which relaxes exponentially at its own characteristic time scale. This is sometimes called the Kohlrausch–Williams–Watts relaxation law.

There are many ways to measure the time-domain IP effect in field studies and a number of different expressions have appeared in the literature. Let $V(t_0)$ be the voltage measured at some fixed time t_0 after switch-off. The *polarizability* η [mV/V] of the ground has been defined as

$$\eta = \frac{V(t_0)}{V_0}. \tag{5.1}$$

The *partial chargeability* M_{12} [ms] of the ground is its polarizability averaged over a predefined time window $[t_1, t_2]$ during the stretched exponential decay,

$$M_{12} = \frac{1}{V_0}\int_{t_1}^{t_2} V(t)dt. \tag{5.2}$$

There is a considerable amount of inconsistency throughout the geophysical literature with respect to the exact definitions of η and M_{12}. Equations (5.1) and (5.2) are commonly used, but other definitions and nomenclature have been adopted by different authors.

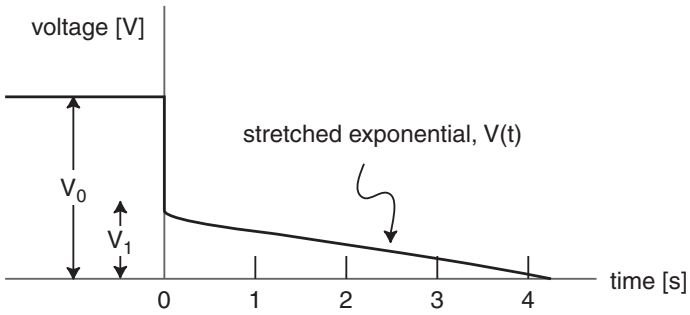

Figure 5.2 A typical IP decay curve.

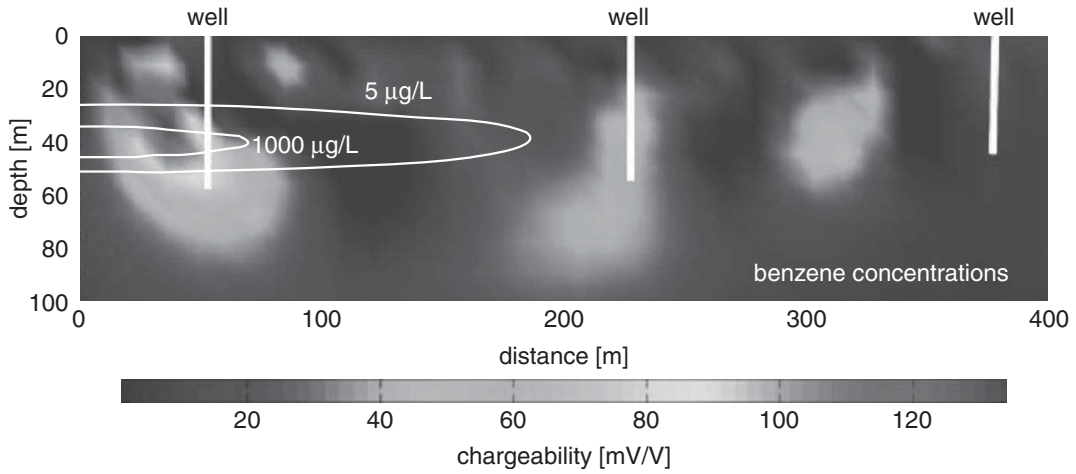

Figure 5.3 IP response of a benzene contaminant plume, Cape Cod, Massachusetts, along with contours of benzene concentration. After Sogade *et al*. (2006).

Example. IP mapping of a benzene contaminant plume.

The Massachusetts Military Reservation on Cape Cod was used as a US Air Force facility from 1948–1973. Following an uncontrolled release of jet fuel, a subsurface plume of volume 265 m^3 and length 1.5 km consisting of benzene and other organic contaminants was detected and initially characterized during the 1980s. Groundwater wells in 1996 showed benzene concentrations as high as 2500 μg/L. The geology is glacial outwash sands and gravels underlain at ~ 60 m depth by clayey lacustrine sediments. A number of laboratory-scale studies on contaminated rock and soil samples (e.g. Vanhala *et al*., 1992) have found that significant IP anomalies are associated with organic compounds such as benzene, toluene, and trichloroethene. Accordingly, time-domain IP field-scale data were acquired on-site (Sogade *et al*., 2006) in order to map the spatial extent of the plume. The two-dimensional (2-D) depth section of chargeability shown in Figure 5.3 was constructed from an IP measurement profile in the dipole–dipole configuration of total length 560 m with 24-m electrode spacing. Chargeability is defined in this study as the ratio V_1/V_0 shown in Figure 5.2, which by the definition (5.1) is essentially the polarizability η at time $t_0 = 0$. Notice that the zone of highest chargeability (~ 130 mV/V) shows a very good spatial correlation with the region of highest benzene concentration as determined by sampling of groundwater wells.

In the frequency-domain IP method, an alternating current I of frequency f, generally in the range 1 mHz–1 kHz, is injected into the ground. An IP effect is also frequently observed in the frequency domain; it appears as an out-of-phase component of electrical conduction at low frequencies (Vinegar and Waxman, 1984). Using any electrode configuration, a measure of the IP effect in the CRIU is the *percentage frequency effect PFE* defined by

$$PFE = 100\,\frac{\rho_a(f_1) - \rho_a(f_2)}{\rho_a(f_2)} \tag{5.3}$$

In Equation (5.3), $\rho_a(f_1)$ and $\rho_a(f_2)$ are the apparent resistivities measured at two frequencies f_1 and f_2 such that $f_1 < f_2$. Recall from the previous chapter that the apparent resistivity at frequency f is given by the formula

$$\rho_a = K\frac{V}{I} = KZ, \tag{5.4}$$

where K is the geometric factor of the electrode configuration and $Z = V/I$ is the impedance. In principle, any convenient electrode-array configuration can be selected for IP measurements. However, the suitability of a given array depends on a number of factors including the signal-to-noise ratio, site geology, electromagnetic-induction coupling effects at frequencies higher than ~ 100 Hz (Revil *et al*., 2012), and, as described later, electrode polarization effects. These factors are best explored by detailed forward modeling.

A second measure of the IP effect in the frequency domain is the *phase angle* ϕ [mrad] defined, at frequency f, to be the small difference in the phase of the measured voltage with respect to that of the injected current. Note that the phase of the voltage lags behind that of the causative current. In terms of the phase angle, the impedance $Z = V/I$ in Equation (5.4) has the form $Z = |Z|\exp(-i\phi)$. Inserting this expression into Equation (5.4), multiplication by the known array geometric factor K, and finally taking the reciprocal results in

$$\sigma^* = \frac{\exp(i\phi)}{K|Z|} = |\sigma|\exp(i\phi) = \sigma' + i\sigma''; \tag{5.5}$$

where σ^* is conventionally termed the *complex conductivity*. Note that the real and imaginary parts of the complex conductivity are related by

$$\sigma'' = \sigma'\tan\phi. \tag{5.6}$$

In field surveys, the complex conductivity (or equivalently, the amplitude $|\sigma|$ and phase angle φ) is measured at a single frequency. The quantity $\rho^* = 1/\sigma^*$ termed the *complex resistivity* is also frequently mentioned in the literature. The *spectral IP* (SIP) method is essentially a measurement of complex resistivity ρ^* over a range of frequencies. The SIP method is the analogous field-scale geophysical technique to AC impedance spectroscopy or dielectric spectroscopy measurements made in the laboratory on rock samples generally at higher frequencies.

5.2 Phenomenological resistivity dispersion models

A large number of empirical models have been developed to describe the frequency dependence of the electrical resistivity of polarizable geomaterials. Perhaps the simplest is the Debye model that describes a highly idealized medium relaxing according to a single exponential time decay, i.e. $V(t) = V_0 m\exp(-t/\tau)$. In the frequency domain, the Debye complex resistivity $\rho^*(\omega)$ is

$$\rho^*(\omega) = \rho_0\left[1 - m\left(1 - \frac{1}{1 + i\omega\tau}\right)\right], \tag{5.7}$$

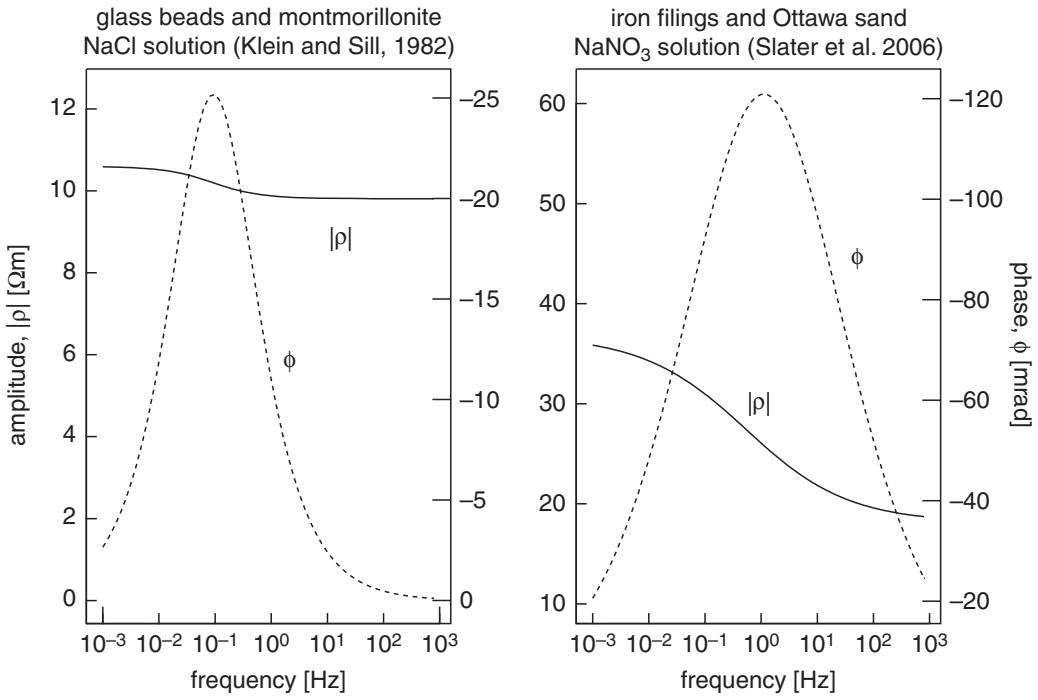

Figure 5.4 Cole–Cole complex electrical resistivity spectra.

where ρ_0 is the DC resistivity at zero frequency. The parameters m and τ [s] are termed the chargeability and relaxation time constant, respectively.

More widely used and applicable to heterogeneous geomaterials is the Cole–Cole phenomenological model (Cole and Cole, 1941; Pelton *et al*., 1978) written in the form

$$\rho^*(\omega) = \rho_0\left[1 - m\left(1 - \frac{1}{1 + (i\omega\tau_0)^c}\right)\right], \tag{5.8}$$

with frequency exponent c. The Cole–Cole model describes a material that relaxes according to a heavy-tailed distribution $g(\tau)$ of relaxation times. The distribution function $g(\tau)$ is bell-shaped and symmetric about τ_0 (Revil *et al*., 2012).

The values of the parameters m, τ_0, and c in Equation (5.8) for a given geomaterial are typically determined by a fit to experimental measurements of electrical properties made in the laboratory. For example, Klein and Sill (1982) report $m = 0.075$, $\tau_0 = 1.8$ s, $c = 0.72$ and $\rho_0 = 10.6$ Ωm for the best fit to electrical resistivity measurements over the frequency range 1 mHz–1 kHz on a mix of glass beads and montmorillonite saturated with a 0.01 mol NaCl solution. Slater *et al*. (2006b) report $m = 0.51$, $\tau_0 = 0.33$ s, $c = 0.424$ and $\rho_0 = 36.9$ Ωm for electrical resistivity measurements between 0.1 Hz–1 kHz on 10 wt.% iron filings mixed with Ottawa sand and saturated with a 0.01 mol $NaNO_3$ solution. The Cole–Cole electrical spectra using these parameters are shown in Figure 5.4. The Cole–Cole model (5.8) is phenomenological in the sense that its parameters m, τ_0, and c are not intended to be derived from basic physical arguments.

An equivalent electrical circuit (Dias, 2000) for the Cole–Cole dispersion model provides an intuitive conceptualization of the frequency-domain IP effect. The equivalent circuit is shown in Figure 5.5, where

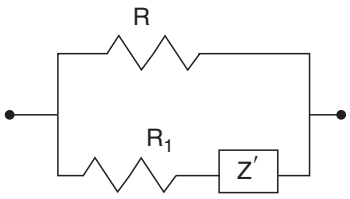

Figure 5.5 Equivalent electrical circuit for the Cole–Cole model.

$$m = \frac{R}{R + R_1}; \quad \tau = \left(\frac{R + R_1}{a}\right)^{\frac{1}{c}}; \quad Z' = \frac{a}{(i\omega)^c}; \tag{5.9}$$

and the frequency exponent obeys $0 \leq c \leq 1$. Note that the circuit contains a parallel combination of a purely resistive path R, corresponding to quasi-free ionic charge migration, and a second path of resistance R_1 and impedance Z', corresponding to charge accumulation (polarization) at subsurface interfaces. A large number of other phenomenological dispersion models, including various generalizations of the Cole–Cole function (e.g. Kruschwitz *et al*., 2010), have been proposed over the past several decades to explain IP observations. Equivalent electrical circuits for many of these models, which can become quite complex, are tabulated by Dias (2000).

5.3 Electrode, membrane, and interfacial polarization

The IP effect, measured in either the time or frequency domain, is considered by many geophysicists to be understood as follows. Suppose an electric current is caused to flow within the ground as a result of a voltage applied across a pair of current electrodes. Consider a subsurface interface, such as one between the pore-fluid electrolyte and a charged mineral surface. Such a junction is associated with contrasts in conduction mechanisms and charge-carrier mobilities, and therefore it acts as an electrochemical impedance to current flow. Charges accumulate at or near the mineral–electrolyte interface. In effect, the ground becomes polarized. In this manner, the continuous application of current from the external source forces the system into a non-equilibrium steady state in which charge distributions are built up at mineral–electrolyte interfaces. The charge distributions dissipate once the driving current is switched off.

At IP frequencies, several important mechanisms of subsurface charge accumulation, namely, *electrode polarization*, *membrane polarization*, and *interfacial polarization* have been discussed in the literature (e.g. Olhoeft, 1985). Electrode polarization is found in rocks containing mineral grains of high electrical conductivity. Metallic grains, for example, can partially block or otherwise impede the movement of ions within the pore-fluid electrolyte. The primary conduction mechanism is electronic on the metal side and ionic on the electrolyte side of a metal–electrolyte junction. Electrons are transferred across

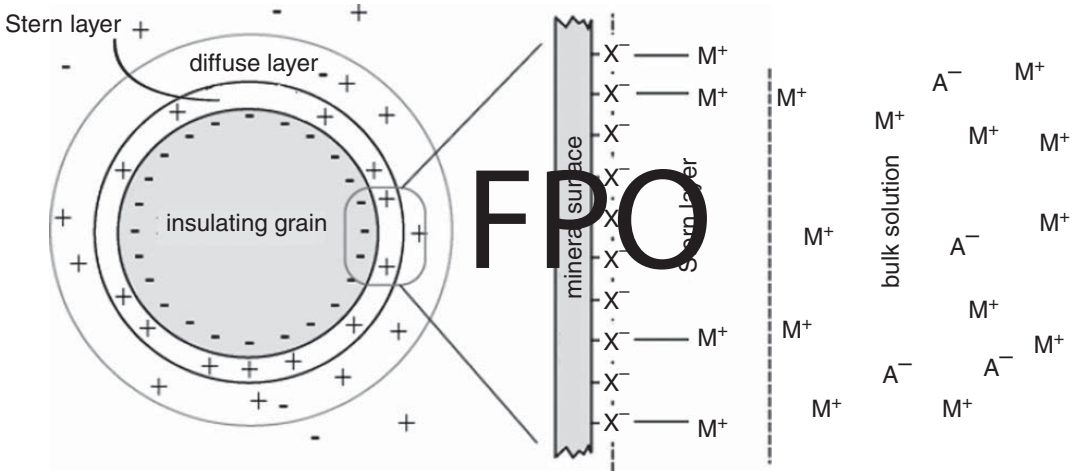

Figure 5.6 The electric double layer at the clay-mineral–electrolyte interface. After Revil and Florsch (2010).

the interface via oxidation–reduction chemical reactions. However, an energy barrier must be overcome in order for the electron transfer to proceed. It is this barrier that causes charges to accumulate at the junction, and thus an electrochemical impedance appears at metal–electrolyte interfaces.

In membrane polarization, the mobility of ions in relatively constricted pores is impeded by less-mobile ions. This can occur when electric current is passed through sediments in which clay is dispersed among larger mineral grains. Consider first the equilibrium case prior to excitation of the system by an external current. The surface of clay minerals is negatively charged. The negative surface charges attract cations from the pore-fluid electrolyte. As shown in Figure 5.6, some of these cations attach weakly to the mineral surface, contributing to the *fixed*, or *Stern layer*. Other cations form a second *diffuse*, or *Guoy–Chapman layer* within the bulk solution. The fixed and diffuse layers comprise the *electric double layer* (e.g. Parsons, 1990; Delgado *et al*., 2005) that is basic to much of electrochemistry.

Now suppose an external current is applied. The relatively poor mobility of anions and cations in the electric double layer, as shown in the figure, impedes the transport of the externally mobilized, ionic charge carriers. The magnitude of the impedance depends on the size and polarity of the charge carriers. In this manner, clay particles act as ion-selective membranes, passing some charge carriers relatively easily while preferentially impeding others. Leroy *et al*. (2008) have further suggested that the Stern layer becomes polarized when an external current is applied, without an accompanying charge buildup in the diffuse layer.

A third type of polarization, interfacial polarization or the *Maxwell–Wagner effect*, can become important at relatively high IP frequencies, greater than 1 kHz (Hizem *et al*., 2008). Interfacial polarization is a purely physical effect caused by electric charges that accumulate at conductivity interfaces within a heterogeneous medium as it is subjected to an applied electric field. We shall see in Chapter 9 that a closely related phenomenon, interfacial dielectric polarization in which charges accumulate at permittivity interfaces, can be important at the low end of ground-penetrating radar (GPR) frequencies.

5.4 IP response and subsurface geological processes

Since the IP effect originates at fluid–grain interfaces, a body that contains widely disseminated metallic or clay minerals should generate a larger IP response than a massive body containing the same total volume of metal or clay. Vinegar and Waxman (1984) report that the IP response is proportional to shaliness, a measure of the clay content, of sandstones. Slater *et al*. (2006b) have investigated in the laboratory both metal–sand and clay–sand mixtures, exhibiting electrode and membrane polarization respectively. They find that a critical parameter controlling the size of the IP effect in both cases is, indeed, the interfacial geometric factor S_p [1/μm]. As described by Pape *et al*. (1987), the factor S_p is the surface area of the mineral grains per unit volume of the saturating fluid; in other words, it is a measure of the mineral surface area that is in contact with pore electrolyte. Slater *et al*. (2006b) show that the IP response increases with the parameter S_p. The relationship $\sigma'' \sim S_p^{0.74}$ provides a good fit to data compiled from the literature by Kruschwitz *et al*. (2010), as shown by the dotted line in Figure 5.7.

A number of authors (e.g. Lesmes and Morgan, 2001; Titov *et al*., 2002) have attempted to develop first-principle theoretical models that can be used to interpret complex resistivity spectra in terms of pore microstructure and grain-size distributions, with possible implications for inferring hydraulic properties such as permeability. These models have been partially successful but this remains an area of active research. Kruschwitz *et al*. (2010), taking a phenomenological approach, suggest that small pores should lead to faster relaxation of charge polarization and hence small values of the time constant τ_0 in the Cole–Cole equation (5.8). Larger pores would lead to slower relaxation and larger values of τ_0. A number of other attempts have been made to ascribe physical meaning to the Cole–Cole parameters (e.g. Revil *et al*., 2012).

Following early studies by Olhoeft (1986) and others, there has been fast-growing interest in the application of IP field geophysical methods to characterize subsurface

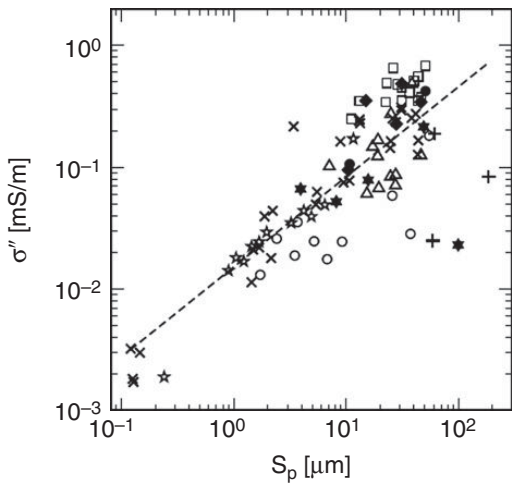

Figure 5.7 Imaginary conductivity as a function of interfacial geometric factor S_p for different geomaterials. After Kruschwitz *et al*. (2010).

organic contaminant plumes and other complex biogeochemical environments. The work of Sogade *et al*. (2006) was described earlier in this chapter. More recently, the spectral IP method was used successfully (Williams *et al*., 2009) to monitor the biostimulated subsurface activity of microorganisms that reduce metallic iron and sulfate minerals in contaminated groundwater. A primary action of the microorganisms is to convert metallic minerals into a non-metallic sulfide precipitate and hence decrease the magnitude of subsurface electrode polarization. (Doherty *et al*., 2010) used the IP method in the Wenner-array configuration (electrode spacing $a = 2.0$ m) in conjunction with self-potential, resistivity, and electromagnetic-induction geophysical data to help characterize an organic contaminant plume beneath an abandoned gasworks site in Northern Ireland. The observed chargeability anomalies were explained in terms of an electrochemical model in which ions and electrons are transferred across a thin clay layer separating perched wastewater from the underlying, biodegrading contaminant plume.

5.5 Non-polarizing electrodes

The difference in electric charge transport mechanism between the soil pore-fluid electrolyte and the metal electrodes staked into the ground results in an electrochemical impedance mismatch at the metal–electrolyte interface. If electric current passes in one direction between the soil and the electrode for an extended period of time, charge accumulates at the interface manifesting itself as an electrode polarization. The result is a spurious DC voltage. It is easy to misinterpret the spurious DC voltage as an apparent chargeability of the subsurface. The polarizability of a metal electrode depends on the type of metal employed, as shown in the study by LaBrecque and Daily (2008).

Non-polarizing electrodes reduce the electrochemical mismatch, and hence mitigate the spurious contribution to electrode polarization. Essentially, a non-polarizing electrode is one whose potential does not change upon the passage of an electric current (Bard and Faulkner, 1980). Typical materials used in the fabrication of non-polarizing electrodes are $Pb/PbCl_2$ and $Cu/CuSO_4$. The metal electrode is enclosed within a porous medium or a hard gel that is infused with a solution containing a salt of the same metal. The salt solution buffers the transition from electronic conduction in the metal electrode to ionic conduction in the soil electrolyte. The electric potential of carefully made $Pb/PbCl_2$ non-polarizing electrodes, such as those described by Petiau (2000), remains stable over time frames lasting months to years.

5.6 IP illustrated case history

Archaeological investigation of paleometallurgical activities.

The mine of Castel-Minier in France was an important source of iron, lead, and silver during the Middle Ages. Originating as a by-product of smelting, relic slag heaps contain a

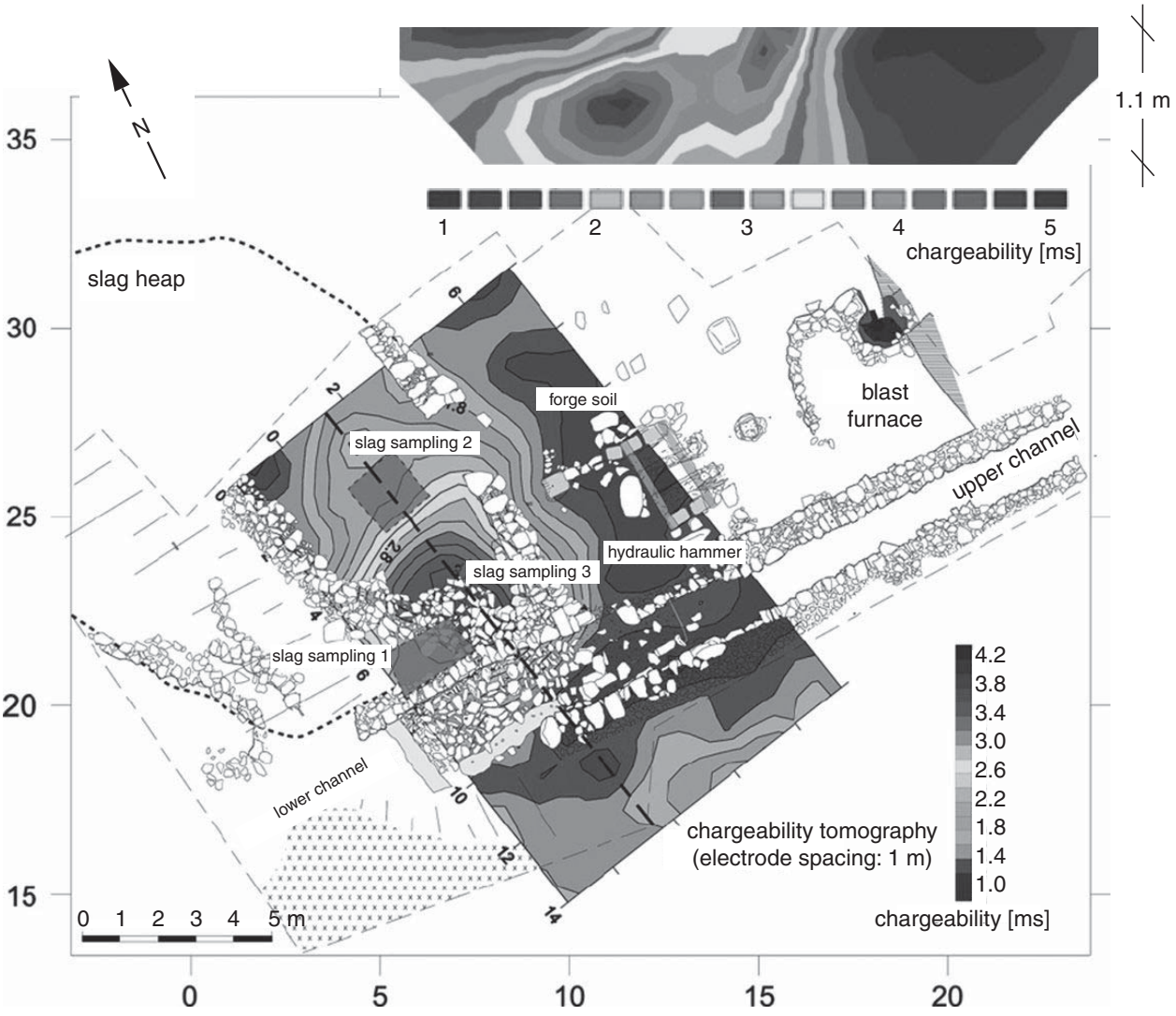

Figure 5.8 Apparent intrinsic chargeability map and vertical cross-section in support of a paleometallurgical investigation. The location of the cross-section corresponds to the dotted line on the map. After Florsch *et al.* (2010).

wealth of information of interest to metallurgical archaeologists. Of primary interest is to make a determination of the total volume of slag so that the productivity of the former mining operations can be assessed. Slag heaps contain magnetite and other metallic minerals and consequently make an excellent IP target on the basis of electrode polarization. An apparent *intrinsic chargeability* map, including a vertical cross-section, based on the IP survey conducted by Florsch *et al.* (2011) using a Wenner array (electrode spacing $a = 1.0$ m) is shown in Figure 5.8. The intrinsic chargeability m is defined in this study as the partial chargeability M_{12} between $t_1 = 10$ ms and $t_2 = 30$ ms, multiplied by $\Delta t = t_2 - t_1 = 20$ ms, so that $m = M_{12}\Delta t$. The buried slag is easily identified as the zone of high intrinsic chargeability with $m > 3$ ms. The map also shows the spatial relation of the slag heap in the larger context of the site archaeological excavation. Based on a calibration of the IP response from slag sampled from the three shaded regions in the figure, Florsch

et al. (2011) have demonstrated that the slag content increases in proportion to its apparent chargeability. A detailed analysis shows that the sixteenth-century mine produced ~ 7.6 tons of slag, corresponding to ~ 6.9 tons of commercial iron.

5.7 Self-potential (SP): introduction

Under natural conditions, without any introduction of an artifical current into the ground as in the resistivity/IP methods, various modes of electric charge imbalance or accumulation are found to spontaneously develop in the subsurface (Jouniaux *et al*., 2009). The resulting self-potentials, which can be measured using pairs of electrodes deployed at the surface or less commonly in boreholes, are very stable in time and are generally in the range of ± 100 mV or higher. A voltmeter is used to measure the SP signals; it should have a high sensitivity (0.1 mV) and a high input impedance (typically >100 MΩ) compared to that of the ground between the two electrodes.

In near-surface applications, commonly, one of the electrodes is held at a fixed location and used as a base or reference station while the other electrode is moved from place to place across an area under investigation. The potential difference between the roving electrode and the reference electrode is the quantity that is measured. In more sophisticated setups, a multi-electrode array of electrodes can also be deployed for monitoring the spatiotemporal changes in SP signals across the survey area. In such cases, the potentials at the various electrodes comprising the array, relative to the potential of the fixed electrode, are recorded periodically by a multiplexed voltmeter.

Self-potential data should always be corrected prior to interpretation for temporal drift and topographic effects (Zhou *et al*., 1999). A topographic correction is required since SP signals tend to increase in the downhill direction, along the local hydraulic gradient. It has also been commonly observed that SP readings are noisier in heavily vegetated areas, relative to sparsely vegetated areas, due to bioelectric activity. To ensure good electrical contact with the ground, electrodes can be inserted into shallow augured holes filled with a mud slurry.

Example. SP mapping of the groundwater system at Stromboli volcano.

An SP survey conducted on the persistently active Stromboli volcano in the Tyrrhenian Sea, Italy, is reported by Finizola *et al*. (2006) with the goal to identify subsurface groundwater flow patterns. Detection of aquifers on volcanic islands is required for improved water-resource management and also better hazard assessment since water can react violently with magma and cause dangerous phreatic eruptions. The SP data with 20-m station spacing are shown in Figure 5.9 along with a co-located 2-D inversion of resistivity data using the Wenner electrode configuration (see Chapter 4). The hydrothermal system beneath Stromboli summit is easily recognized by the strong SP variations within the region of lowest resistivity, i.e. the rightmost shaded region marked C on the figure.

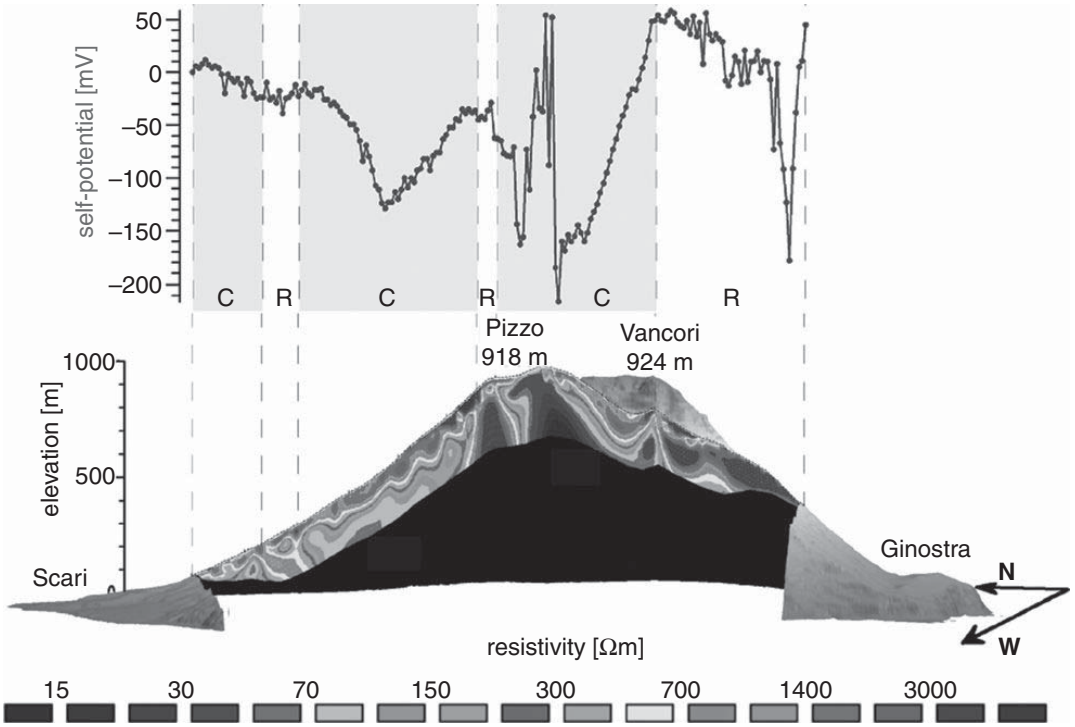

Figure 5.9 SP signals and 2-D electrical resistivity structure at Stromboli volcano, Italy. C = conductive zone; R = resistive zone. After Finizola *et al*. (2006).

5.8 Physical mechanisms

Subsurface charge accumulations may be sustained by a number of physical and electrochemical processes. Large SP anomalies, up to hundreds of mV, for example, have long been measured in association with zones of metal sulfide and oxide mineralization. An enduring theory purporting to explain the so-called *mineralization potential* of sulfide bodies is due to Sato and Mooney (1960). Stable SP anomalies of comparable magnitude may also be registered in the presence of metallic cultural noise such as pipelines, steel well casings, metallic fences, and utility boxes (Revil *et al*., 2012). This type of SP signal is caused by the movement of electrons in response to spatial variations in the redox potential at heterogeneous metal–electrolyte interfaces.

Another common mechanism that generates a spontaneous potential involves the movement of electrolytic groundwater through a porous rock. A *streaming potential*, for example, develops when pore-fluid electrolyte flows in response to a pressure and/or thermal gradient. Due to the presence of the electric double layer at the mineral surface (Figure 5.6), the fluid flow carries an excess of the mobile counter ions resident in the bulk electrolyte, relative to a deficit of ions of the opposite sign that constitute the immobile fixed layer. This differential movement of ions and counter ions is equivalent to an electric

current. An effective resistance to the current is provided by the electrolyte viscosity η, its resistivity ρ, and the *zeta potential* ζ (the potential difference between the charged mineral surface and an arbitrary point within the neutral bulk electrolyte). The streaming potential is nothing more than the resulting electrical potential drop between two points along the path of the fluid flow (e.g. Rice and Whitehead, 1965; Levine *et al*., 1975). A streaming potential of this type often arises as pore electrolytes flow in response to an external mechanical disurbance; this constitutes the fundamental basis for the *seismoelectric effect* to be discussed in Chapter 10.

A different type of SP effect occurs at the liquid–liquid interface between two pore fluids that are characterized by different concentrations of ions in solution. There will be a net transfer of ions across the junction as the more-concentrated solution diffuses into the less-concentrated solution. Since cations and anions generally have different mobilities, the rates of diffusion of the different charged species across the interface are unequal. The differential movement of ions leads to the development of a net charge distribution on the liquid–liquid interface, thereby generating a liquid junction or *diffusion potential*. A sharp contrast in solution concentration is not required, as a diffusion potential can also occur in the presence of a salinity gradient.

It has long been recognized in geophysical well-logging that a spontaneous potential develops at junctions between permeable sand and less-permeable shale beds. Suppose the pore fluid is an ideal electrolyte consisting of NaCl only. Due to its layered clay structure and charged mineral surfaces, the shale is somewhat permeable to the Na^+ cations but it is relatively impervious to the Cl^- anions. Suppose the shale bed separates two sand beds which contain different NaCl concentrations. There will be a net migration of Na^+ cations across the shale bed from the more-concentrated toward the less-concentrated solution. Since shales preferentially pass the cations and restrict the anions, they act much like an ion-selective membrane (Bard and Faulkner, 1980). The differential movement of ions in shale beds generates the *membrane potential* that is measured by a downhole voltmeter.

The *thermoelectric effect* can also be a significant source of SP signals in geothermal systems, volcanoes, near-underground coal fires, and in other geological settings that are characterized by persistent spatial variations in subsurface temperature. The thermoelectric effect is the appearance of a voltage across a sample of geomaterial that is not of a uniform temperature. A temperature gradient causes mobile charge carriers within the geomaterial to migrate from regions of elevated temperature to regions of cooler temperature. The differential movement of charge carriers of different species establishes a non-uniform subsurface charge distribution. The thermoelectric coupling coefficient [mV/°C] is defined as the ratio $\Delta V/\Delta T$ of the voltage to temperature difference. Zlotnicki and Nishida (2003) report values of the order of ~ 0.1–1.0 mV/°C.

Finally, Minsley *et al*. (2007) have shown that subsurface spatial variations in electrical conductivity can also have an effect on potential measurements made at the surface. However, it is often difficult to estimate the magnitude of this effect in practical situations since the underground distribution of electrical conductivity is rarely known.

5.9 Interpretation of SP measurements

Since SP signals are generated by equal and opposite charge distributions, as indicated schematically in Figure 5.1, an SP source may be modeled as an assemblage of electric dipoles. Recall that an electric dipole is the simplest possible distribution of equal and opposite charge, namely a positive point charge q and a negative point charge $-q$ separated by a distance d. The electric dipole moment is given by $m = qd$. A polarized sphere, in which the positive charge is distributed over one hemisphere and the negative charge is distributed over the other hemisphere, may be represented at large distances relative to its radius by an equivalent electric dipole of moment M.

Polarized sphere. It is straightforward to calculate the electric potential due to a polarized sphere. As shown in Figure 5.10a, suppose the sphere is polarized in the vertical plane $y = 0$ in a direction that makes angle α with respect to the x-axis so that

$$\mathbf{M} = M\cos\alpha\,\hat{\mathbf{x}} + M\sin\alpha\,\hat{\mathbf{z}}. \tag{5.10}$$

The electric potential V of an equivalent electric dipole of moment $\mathbf{M}$ is given by the standard formula (e.g. Blakely, 1995)

$$V = -\frac{\mathbf{M}\cdot\nabla}{4\pi\varepsilon_0}\frac{1}{R} \tag{5.11}$$

where $\varepsilon_0 = 8.85 \times 10^{-12}$ F/m is the permittivity of free space and

$$R = |\mathbf{r}_P - \mathbf{r}_Q| = \sqrt{(x - x_0)^2 + z_0^2} \tag{5.12}$$

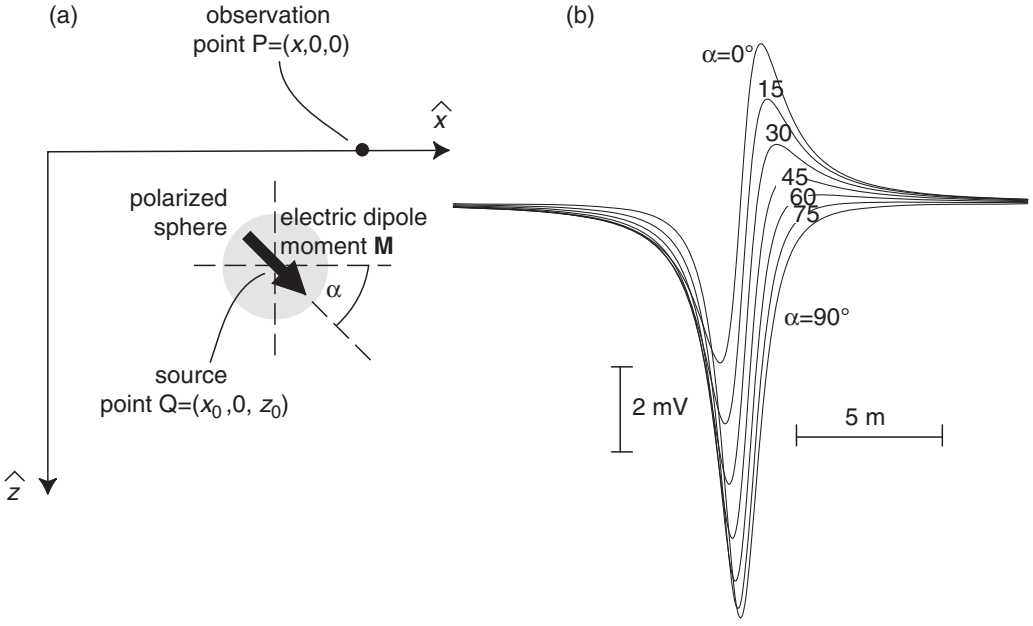

Figure 5.10 (a) A polarized sphere modeled as an electric dipole. (b) The SP response of a buried polarized sphere for different angles of polarization.

is the distance between the dipole at source location $Q = (x_0, 0, z_0)$ and the observation point at Earth's surface, $P = (x, 0, 0)$. Inserting Equations (5.10) and (5.12) into Equation (5.11) results in

$$V(x) = \frac{M}{4\pi\varepsilon_0} \frac{(x - x_0)\cos\alpha - z_0 \sin\alpha}{[(x - x_0)^2 + z_0^2]^{3/2}}. \tag{5.13}$$

The function $V(x)$ is plotted in Figure 5.10b for different values of the angle of polarization from $= 0°$, aligned with the $+x$-axis, to $\alpha = 90°$, aligned with the $+z$-axis. The sphere is buried at depth $z_0 = 1.0$ m and located at $x_0 = 0$. The dipole moment is $M = 10^6$ Cm. Finding a similar analytic solution for the SP response of a long horizontal cylinder is left as an exercise for the reader.

Polarized dipping sheet. Another simple geological scenario for which the SP response is amenable to an analytic treatment is fluid flow within a dipping planar fault structure. The fault plane can be modeled as an electrically polarized thin sheet, or ribbon, of half-width a embedded in a host medium of uniform resistivity ρ (Paul, 1965), as shown in Figure 5.11a. One edge of the sheet is represented as a line of negative charges of density $-\Sigma$ [C/m] while the other is a line of positive charges of density $+\Sigma$ [C/m]; both lines extending from $-\infty$ to $+\infty$ in the along-strike ($\pm y$) direction.

The electric potential V due to a line of charges has the well-known logarithmic form (e.g. Blakely, 1995)

$$V_{\pm} = \pm\frac{\Sigma\rho}{\pi} \ln\left(\frac{1}{r_{\pm}}\right), \tag{5.14}$$

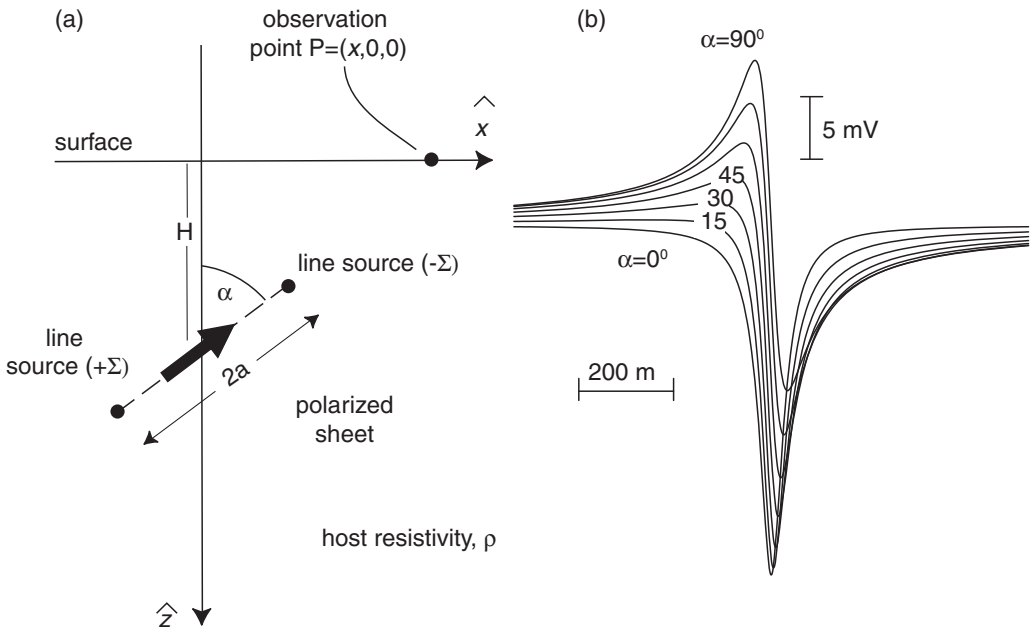

Figure 5.11 (a) A polarized, inclined sheet modeled as an electric line charges. (b) The SP response of a buried polarized sheet for different angles of inclination.

where $r_{\pm}$ is the distance from the observation point to the positive and negative line of charges, respectively. A glance at the geometry in the figure shows that

$$r_{-} = \sqrt{(x - a\cos\alpha)^2 + (H - a\sin\alpha)^2}; \tag{5.15}$$

$$r_{+} = \sqrt{(x + a\cos\alpha)^2 + (H + a\sin\alpha)^2}; \tag{5.16}$$

from which it readily follows

$$\ln\left(\frac{1}{r_{-}}\right) = -\frac{1}{2}\ln[(x - a\cos\alpha)^2 + (H - a\sin\alpha)^2]; \tag{5.17}$$

$$\ln\left(\frac{1}{r_{+}}\right) = -\frac{1}{2}\ln[(x + a\cos\alpha)^2 + (H + a\sin\alpha)^2]. \tag{5.18}$$

The total SP signal due to the two lines of charges is the sum of the potentials due to each sheet, namely, $V = V_{+} + V_{-}$. Adding the two contributions using the above equations results in

$$V = \frac{\Sigma\rho}{2\pi}\left\{\ln[(x - a\cos\alpha)^2 + (H - a\sin\alpha)^2] - \ln[(x + a\cos\alpha)^2 + (H + a\sin\alpha)^2]\right\}, \tag{5.19}$$

which is plotted at Figure 5.11b for different values of the angle α. The following parameters are used: $\Sigma = \pm 0.01$ C/m, $\rho = 10.0$ Ωm, fault-zone half-width $a = 10$ m, and depth of burial $H = 30$ m.

A number of rules can be inferred from the analytic solutions which relate the width of an SP anomaly to the depth of an idealized source. For example, it is easy to show that the depth to a point charge is given by $d = x_{0.5}/\sqrt{12}$, where $x_{0.5}$ is the FWHM of the corresponding SP anomaly, i.e. its width at one-half its maximum value. Similarly, the depth rule for a vertically polarized sphere is $d \sim 0.65x_{0.5}$.

Self-potential surveys often provide useful hydrological information about fractures and karst conduits since streaming-potential anomalies have long been associated with divergent groundwater flow (Lange and Barner, 1995). As illustrated schematically in Figure 5.12, residual SP anomalies, after drift and topographic corrections have been made, are generally positive over groundwater discharges at springs and negative over groundwater infiltration at sinkholes.

5.10 Continuous wavelet transform analysis

The continuous wavelet transform (CWT) was introduced in Chapter 2 as a means for analyzing non-stationary data series. In this section we will see that the CWT can also be used for interpreting potential field measurements in terms of the geometry of the causative source and its depth of burial. The underlying theory is developed in Moreau *et al*. (1997, 1999) and has since been applied to many types of geophysical data including magnetics by Vallee *et al*. (2004). Here we outline the application of CWT for analysis of SP data

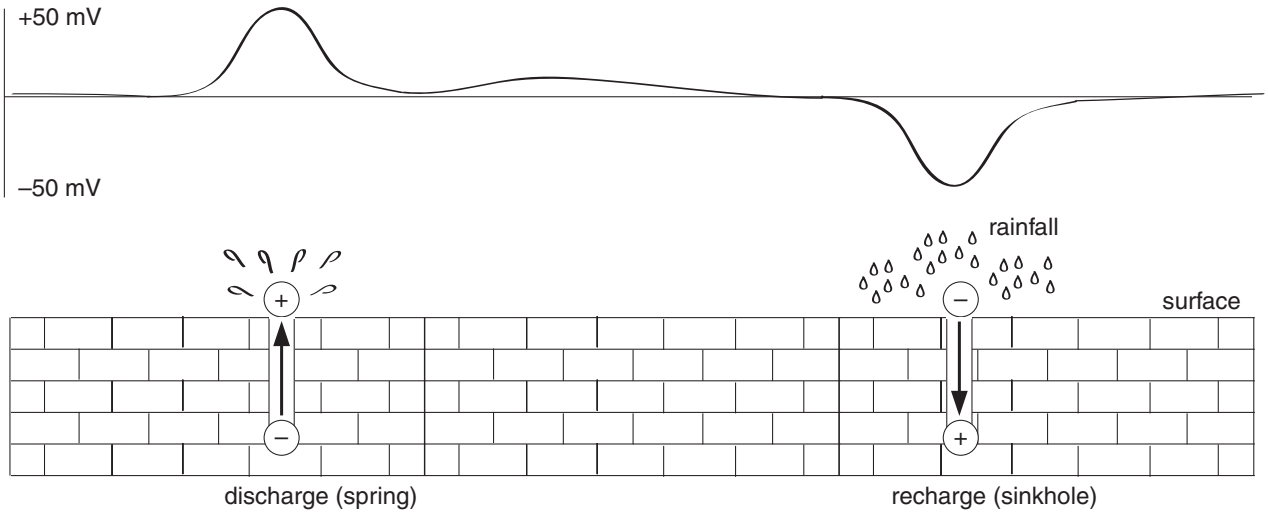

Figure 5.12 (Top) Schematic illustration of streaming-potential residual anomalies associated with groundwater recharge and discharge in karst terrain. (Bottom) The arrows indicate groundwater-flow direction, while the positive and negative symbols indicate equivalent charge polarization.

acquired along a single profile, although the general theory applies to data collected in two spatial dimensions.

To begin, recall that the CWT of an arbitrary one-dimensional function $f(x)$ is given by

$$\tilde{f}(s,t) = \int_{-\infty}^{\infty} dx \frac{1}{s} \psi\left(\frac{x-t}{s}\right) f(x). \tag{5.20}$$

Suppose the function $f(x)$ is a potential field, such as gravity, magnetics, or SP data. Moreau *et al.* (1997; 1999) have shown that a powerful analysis of potential field data is enabled by using a special wavelet $\psi(x)$ that is based on spatial derivatives of the familiar upward continuation operator.

Recall from Equation (3.36) that a potential field $f(x,y,z_0-\Delta z)$ on the level surface $z_0-\Delta z$ can be derived from an upward continuation of measurements of the field $f(x,y,z_0)$ made at the lower level z_0. The formula is

$$f(x,y,z_0-\Delta z) = \int_{-\infty}^{\infty}\int_{-\infty}^{\infty} f(x',y',z_0)\Psi_U(x-x',y-y',\Delta z)dx'dy' \tag{5.21}$$

where the upward continuation operator is

$$\Psi_U(x,y,\Delta z) = \frac{\Delta z}{2\pi}[(x-x')^2+(y-y')^2+\Delta z^2]^{-3/2}. \tag{5.22}$$

Suppose that the potential field is a function of x and z only, i.e. $f = f(x, z)$, which would be the case if the causative body is infinitely extended and uniform in a horizontal strike

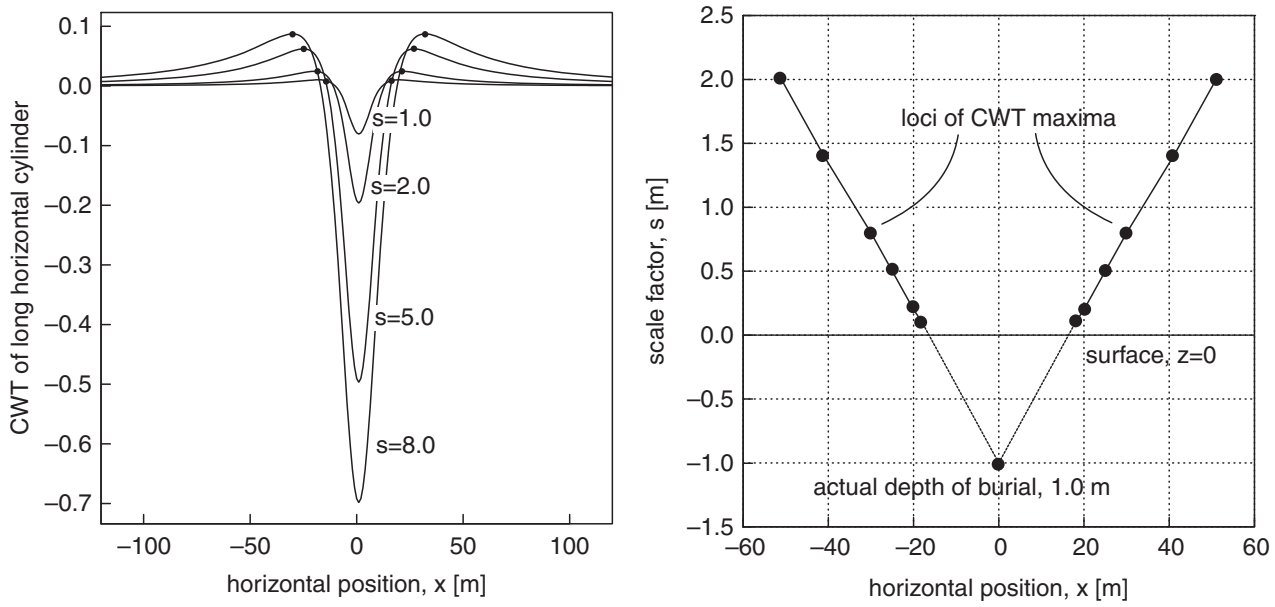

Figure 5.13 (Left) The continuous wavelet transform of a buried long cylinder for various values of *s*, with the symbols marking the maxima. (Right) Straight lines joining the CWT maxima point toward the actual depth of burial of the cylinder.

direction, *y*. In that case, the integration along the strike direction in Equation (5.21) can be carried out analytically with the result

$$\lim_{L\to\infty}\int_{-L}^{L}\frac{dy'}{\left[(x-x')^2+(y-y')^2+\Delta z^2\right]^{3/2}}\sim\frac{2}{(x-x')^2+\Delta z^2}. \tag{5.23}$$

The upward continuation operator therefore simplifies to

$$\Psi_U(x,\Delta z)=\frac{\Delta z}{\pi\left[(x-x')^2+\Delta z^2\right]}. \tag{5.24}$$

The analyzing wavelet for use in Equation (5.20) is the horizontal derivative of the upward continuation operator evaluated at $x'=0$, namely $\psi(x)=\partial\Psi_U/\partial x|_{x'=0}$ or,

$$\psi(x)=\frac{2x\Delta z}{\pi\left[x^2+\Delta z^2\right]^2}. \tag{5.25}$$

A wide range of other analyzing wavelets based on complex linear combinations of horizontal, vertical, and higher-order spatial derivatives of the upward continuation operator can also be selected; the choice Equation (5.25) is highlighted here due to its simplicity.

Using this choice of analyzing wavelet in Equation (5.20), the continuous wavelet transform $\hat{f}(s,t)$ of the SP field due to a long, horizontal cylinder (see Problem 1, below, for the analytic formula) buried at depth $a=1.0$ m and horizontal position $x_0=0$ is shown in Figure 5.13, left. The maxima of the functions $\hat{f}(s,t)$ for different values of s are shown in Figure 5.13, right. If straight lines are formed by joining

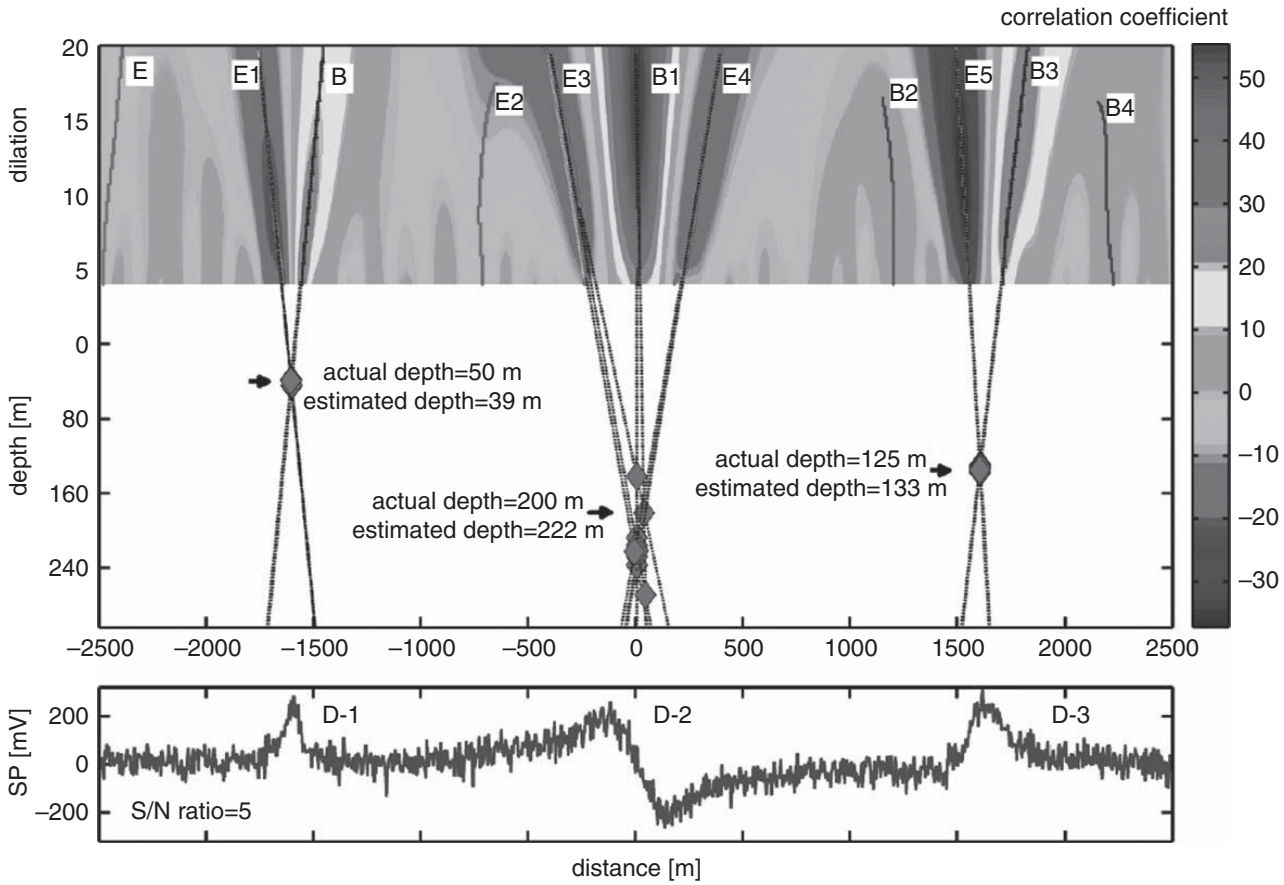

Figure 5.14 Depth determination to SP sources using CWT analysis. After Mauri *et al.* (2010).

together the maxima, they point toward the scale value $s = -a$, which is the burial depth of the cylinder. This example is indicative of a general rule (Moreau *et al.*, 1997; 1999) that the loci of maxima of the continuous wavelet transforms of potential fields converge towards their causative sources. The general rule is valid in $n = 1$, 2, and 3 spatial dimensions and applies to both infinitely extended and compact sources of different shapes.

A more detailed example of source-depth determination using wavelet analysis is shown in Figure 5.14. The bottom plot shows theoretical SP signals [mV] for three electric dipoles, each signal being contaminated by Gaussian-distributed noise with a signal-to-noise (S/N) ratio of 5: D-1 is a horizontal dipole buried at 50 m depth; D-2 is a vertical dipole buried at 200 m; D-3 is inclined at 45° and buried at 125 m. The CWT of the SP signals is shown in the top panel of Figure 5.14. In this example, the second vertical derivative of the upward continuation operator was selected as the analyzing wavelet. The extremal lines (labeled with B and E in the figure) converge to depths marked by the red diamonds in the figure. The scatter in the positions of the red diamonds is caused largely by the presence of the noise in the synthetic SP signals; however, the depths estimated by the CWT analysis are in good agreement with the actual modeled depths.

5.11 SP illustrated case history

Example. SP mapping of an active landslide.

Geoelectrical measurements have become widely used to characterize and monitor active landslides. The SP technique is often used in conjuction with electrical resistivity tomography (ERT) to identify potential slip planes, bedrock surfaces, and zones of fluid discharge and infiltration at sites that are vulnerable to mass movement. Chambers *et al*. (2011) have combined SP, ERT, and conventional geological mapping techniques in their study of an escarpment within the Jurassic mudrocks of northeast England that is triggering earthslides and earthflows. The observed SP signals at this site are caused by streaming potentials associated with downslope groundwater movement.

The SP data were acquired along several transects coincident with 2-D ERT profiles. Non-polarizing Pb/PbCl electrodes were used for both the reference and roving SP electrodes, with 5-m station spacing. Two SP profiles and their co-located resistivity images are shown in Figure 5.15. As a check on repeatability and to estimate temporal drift, SP data were acquired and are shown in the figure for measurements taken in both the upslope (green symbols) and downslope (dark-blue symbols) directions, along with the average readings (solid orange line). The data show good repeatability with a drift of not more than ~ 3 mV. Along both profiles, it is readily seen that the SP signals become more positive with increasing distance downslope. This trend is consistent with a streaming potential caused by groundwater infiltrating at the head of the slope and flowing downslope. The sudden increase in SP values in both profiles is associated with fluid discharge

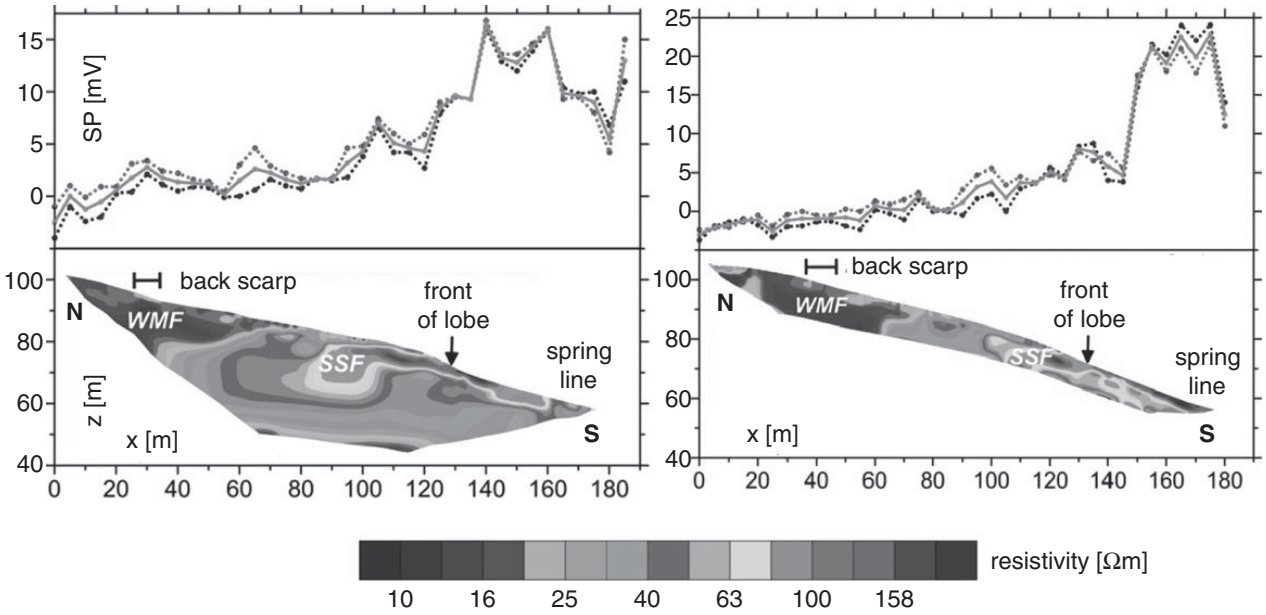

Figure 5.15 SP profiles and co-located 2-D ERT images at an active landslide in northeast England; WMF = Whitby mudstone formation; SSF = Staithes sandstone and Cleveland ironstone formation. After Chambers *et al*. (2011).

though seeps located at the front of the lobe. The SP data are also consistent with the electrical resistivity images, which predominantly reflect lithological variations. For example, the WMF shows low resistivity due to its high clay content. The thin, near-surface zones of high resistivity within the SSF are areas characterized by heterogeneous, well-drained silts and sands. Overall, the combined SP and ERT dataset provides complementary perspectives on, respectively, fluid-flow patterns and the underlying subsurface lithological variations within an active landslide region.

Problem

1. Show that the potential $V(x)$ due to a long horizontal cylinder aligned in the y-direction and buried at location (x_0, z_0) is

$$V(x) = \frac{M'}{2\pi\varepsilon_0} \frac{(x - x_0)\cos\alpha - z_0 \sin\alpha}{(x - x_0)^2 + z_0^2},$$

where M' is the electric dipole moment per unit length and the cylinder is polarized at angle α with respect to the x-axis. Hint: consider the cylinder to be a line of dipoles along the y-axis and integrate the standard dipole formula (5.11) accordingly.